

Adaptive optics with a magnetic deformable mirror: applications in the human eye

Enrique J. Fernández

*Biomedical Imaging Group, Department of Optometry and Vision Sciences, Cardiff University, Wales, UK
Laboratorio de Optica, Universidad de Murcia, Centro de Investigación en Optica y Nanotecnología, Campus de
Espinardo, 30071 Murcia, Spain*
enriquej@um.es

Laurent Vabre

*Laboratoire d'Etudes Spatiales et d'Instrumentation en Astrophysique, Observatoire de Paris-Meudon, 5 Place Jules
Janssen, 92190; Meudon, France*
lvabre@mesioj.obspm.fr

Boris Hermann, Angelika Unterhuber, Boris Považay, Wolfgang Drexler

*Biomedical Imaging Group, Department of Optometry and Vision Sciences, Cardiff University, Wales, UK
HermannB@cardiff.ac.uk, UnterhuberA@cardiff.ac.uk, PovazayB@cardiff.ac.uk, DrexlerW@cardiff.ac.uk*

Abstract: A novel deformable mirror using 52 independent magnetic actuators (MIRAO 52, Imagine Eyes) is presented and characterized for ophthalmic applications. The capabilities of the device to reproduce different surfaces, in particular Zernike polynomials up to the fifth order, are investigated in detail. The study of the influence functions of the deformable mirror reveals a significant linear response with the applied voltage. The correcting device also presents a high fidelity in the generation of surfaces. The ranges of production of Zernike polynomials fully cover those typically found in the human eye, even for the cases of highly aberrated eyes. Data from keratoconic eyes are confronted with the obtained ranges, showing that the deformable mirror is able to compensate for these strong aberrations. Ocular aberration correction with polychromatic light, using a near Gaussian spectrum of 130 nm full width at half maximum centered at 800 nm, in five subjects is accomplished by simultaneously using the deformable mirror and an achromatizing lens, in order to compensate for the monochromatic and chromatic aberrations, respectively. Results from living eyes, including one exhibiting 4.66 D of myopia and a near pathologic cornea with notable high order aberrations, show a practically perfect aberration correction. Benefits and applications of simultaneous monochromatic and chromatic aberration correction are finally discussed in the context of retinal imaging and vision.

©2006 Optical Society of America

OCIS codes: (330.4460) Ophthalmic optics; (010.1080) Adaptive optics; (330.5370) Physiological optics.

References and links

1. N. Hubbin and L. Noethe, "What is adaptive optics?," *Science* **262**, 1345-1484 (1993).
2. H. Hofer, P. Artal, B. Singer, L. Aragón, and D. R. Williams, "Dynamics of the eye's wave aberration," *J. Opt. Soc. Am. A* **18**, 497-506 (2001).
3. E. J. Fernández, I. Iglesias, and P. Artal, "Closed-loop adaptive optics in the human eye," *Opt. Lett.* **26**, 746-748 (2001).
4. H. Hofer, L. Chen, G. Y. Yoon, B. Singer, Y. Yamauchi, and D. R. Williams, "Improvement in retinal image quality with dynamic correction of the eye's aberrations," *Opt. Express* **8**, 631-643 (2001), <http://www.opticsexpress.org/abstract.cfm?URI=OPEX-8-11-631>

5. J. Rha, R. S. Jonnal, K. E. Thorn, J. Qu, Y. Zhang, and D. T. Miller, "Adaptive optics flood-illumination camera for high speed retinal imaging," *Opt. Express* **14**, 4552-4569 (2006), <http://www.opticsinfobase.org/abstract.cfm?URI=oe-14-10-4552>
6. A. W. Dreher, J. F. Bille, and R. N. Weinreb, "Active optical depth resolution improvement of the laser tomographic scanner," *Appl. Opt.* **28**, 804-808 (1989).
7. A. Roorda, F. Romero-Borja, W. J. Donnelly III, H. Queener, T. J. Hebert, and M. C. W. Campbell, "Adaptive optics scanning laser ophthalmoscopy," *Opt. Express* **10**, 405-412 (2002), <http://www.opticsexpress.org/abstract.cfm?URI=OPEX-10-9-405>
8. Y. Zhang, S. Poonja, and A. Roorda, "MEMS-based adaptive optics scanning laser ophthalmoscopy," *Opt. Lett.* **31**, 1268-1270 (2006).
9. B. Hermann, E. J. Fernández, A. Unterhuber, H. Sattmann, A. F. Fercher, W. Drexler, P. M. Prieto, and P. Artal, "Adaptive optics ultrahigh resolution optical coherence tomography," *Opt. Lett.* **29**, 2142-2144 (2004).
10. Y. Zhang, J. Rha, R. S. Jonnal, and D. T. Miller, "Adaptive optics spectral optical coherence tomography for imaging the living retina," *Opt. Express* **13**, 4792-4811 (2005), <http://www.opticsexpress.org/abstract.cfm?URI=OPEX-13-12-4792>
11. R. Zawadzki, S. Jones, S. Olivier, M. Zhao, B. Bower, J. Izatt, S. Choi, S. Laut, and J. Werner, "Adaptive-optics optical coherence tomography for high-resolution and high-speed 3D retinal in vivo imaging," *Opt. Express* **13**, 8532-8546 (2005), <http://www.opticsinfobase.org/abstract.cfm?URI=oe-13-21-8532>
12. E. J. Fernández, B. Považay, B. Hermann, A. Unterhuber, H. Sattmann, P. M. Prieto, R. Leitgeb, P. Ahnelt, P. Artal, and W. Drexler, "Three-dimensional adaptive optics ultrahigh-resolution optical coherence tomography using a liquid crystal spatial light modulator," *Vis. Res.* **45**, 3432-3444 (2005).
13. Y. Zhang, B. Cense, J. Rha, R. S. Jonnal, W. Gao, R. J. Zawadzki, J. S. Werner, S. Jones, S. Olivier, and D. T. Miller, "High-speed volumetric imaging of cone photoreceptors with adaptive optics spectral-domain optical coherence tomography," *Opt. Express* **14**, 4380-4394 (2006), <http://www.opticsinfobase.org/abstract.cfm?URI=oe-14-10-4380>
14. E. J. Fernández, S. Manzanera, P. Piers, and P. Artal, "Adaptive optics visual simulator," *J. Refract. Surgery* **18**, 634-638 (2002).
15. P. Artal, L. Chen, E. J. Fernández, B. Singer, S. Manzanera, and D. R. Williams, "Neural compensation for the eye's optical aberrations," *J. of Vision* **4**, 281-287 (2004), <http://journalofvision.org/4/4/4/,doi:10.1167/4.4.4>.
16. E. J. Fernández and P. Artal, "Study on the effects of monochromatic aberrations in the accommodation response by using adaptive optics," *J. Opt. Soc. of Am. A* **22**, 1732-1738 (2005).
17. P. Piers, E. J. Fernández, S. Manzanera, S. Norrby, and P. Artal, "Adaptive optics simulation of intraocular lenses with modified spherical aberration," *Invest. Ophthalmol. Vis. Sci.* **45**, 4601-4610 (2004).
18. L. Chen, P. B. Kruger, H. Hofer, B. Singer, and D. R. Williams, "Accommodation with higher-order monochromatic aberrations corrected with adaptive optics," *J. Opt. Soc. Am. A* **23**, 1-8 (2006).
19. K. M. Hampson, C. Paterson, C. Dainty, and E. A. H. Mallen, "Adaptive optics system for investigation of the effect of the aberration dynamics of the human eye on steady-state accommodation control," *J. Opt. Soc. Am. A* **23**, 1082-1088 (2006).
20. B. J. Wilson, K. E. Decker, and A. Roorda, "Monochromatic aberrations provide an odd-error cue to focus direction" *J. Opt. Soc. Am. A* **19**, 833-839 (2002).
21. G. Rousset, "Wavefront sensing", NATO ASI Series Vol. C423, 115-137, *Adaptive Optics for Astronomy*, D. Alloin J.-M. Mariotti, Eds., (Kluwer Academic Publishers, 1994).
22. J. Liang, B. Grimm, S. Goelz, and J. F. Bille, "Objective measurement of wave aberrations of the human eye with use of a Hartmann-Shack wave-front sensor," *J. Opt. Soc. Am. A* **11**, 1949-1955 (1994).
23. P. M. Prieto, F. Vargas-Martín, S. Goelz, and P. Artal, "Analysis of the performance of the Hartmann-Shack sensor in the human eye," *J. Opt. Soc. Am. A* **17**, 1388-1398 (2000).
24. F. Vargas-Martín, P. M. Prieto, and P. Artal, "Correction of the aberrations in the human eye with a liquid-crystal spatial light modulator: limits to performance," *J. Opt. Soc. Am. A* **15**, 2552-2562 (1998).
25. P. M. Prieto, E. J. Fernández, S. Manzanera, and P. Artal, "Adaptive optics with a programmable phase modulator: applications in the human eye," *Opt. Express* **12**, 4059-4071 (2004), <http://www.opticsexpress.org/abstract.cfm?URI=OPEX-12-17-4059>
26. J. Liang, D. R. Williams, and D. T. Miller, "Supernormal vision and high-resolution retinal imaging through adaptive optics," *J. Opt. Soc. Am. A* **14**, 2884-2892 (1997).
27. E. Dalimier and C. Dainty, "Comparative analysis of deformable mirrors for ocular adaptive optics," *Opt. Express* **13**, 4275-4285 (2005), <http://www.opticsinfobase.org/abstract.cfm?URI=oe-13-11-4275>
28. G. Vdovin and P. M. Sarro, "Flexible mirror micromachined en silicon," *Appl. Opt.* **29**, 2968-2972 (1995).
29. L. Zhu, P.-C. Sun, and Y. Fainman, "Aberration-free dynamic focusing with a multichannel micromachined membrane deformable mirror," *Appl. Opt.* **38**, 5350-5354 (1999).
30. D. Dayton, S. Restaino, J. Gonglewski, J. Gallegos, S. McDermott, S. Browne, S. Rogers, M. Vaidyanathan, and M. Shilko, "Laboratory and field demonstration of low cost membrane mirror adaptive

- optics system," *Opt. Commun.* **176**, 339-345 (2000).
31. C. Paterson, I Munro, and J. C. Dainty, "A low cost adaptive optics system using a membrane mirror," *Opt. Express* **6**, 175-185 (2000),
<http://www.opticsexpress.org/abstract.cfm?URI=OPEX-6-9-175>
 32. E. J. Fernández and P. Artal, "Membrane deformable mirror for adaptive optics: performance limits in visual optics," *Opt. Express* **11**, 1056-1069 (2003),
<http://www.opticsexpress.org/abstract.cfm?URI=OPEX-11-9-1056>
 33. N. Doble, G. Yoon, L. Chen, P. Bierden, B. Singer, S. Olivier, and D. R. Williams, "Use of a microelectromechanical mirror for adaptive optics in the human eye," *Opt. Lett.* **27**, 1537-1539 (2002).
 34. A. Unterhuber, B. Povazay, B. Hermann, H. Sattmann, W. Drexler, V. Yakovlev, G. Tempea, C. Schubert, E. M. Anger, P. K. Ahnelt, M. Stur, J. E. Morgan, A. Cowey, G. Jung, T. Le, and A. Stingl, "Compact, low-cost TiAl₂O₃ laser for in vivo ultrahigh-resolution optical coherence tomography," *Opt. Lett.* **28**, 905-907 (2003).
 35. American National Standard Institute, American National Standard for Safe Use of Lasers, ANSI Z 136-1 (2000).
 36. C. Boyer, V. Michau, and G. Rousset, "Adaptive optics: interaction matrix measurements and real time control algorithms for the COME ON project," in *Amplitude and Intensity Spatial Interferometry*, Proc. SPIE **1237**, 406-424 (1990).
 37. W. H. Press, S. A. Teukolsky, W. T. Vetterling, and B. P. Flannery, *Numerical Recipes in C*, 2nd ed. (Cambridge Univ. Press, 1992).
 38. E. J. Fernández, A. Unterhuber, B. Povazay, B. Hermann, P. Artal, and W. Drexler, "Chromatic aberration correction of the human eye for retinal imaging in the near infrared," *Opt. Express* **14**, 6213-6225 (2006),
<http://www.opticsexpress.org/abstract.cfm?URI=oe-14-13-6213>
 39. E. J. Fernández, A. Unterhuber, P. M. Prieto, B. Hermann, W. Drexler, and P. Artal, "Ocular aberrations as a function of wavelength in the near infrared measured with a femtosecond laser," *Opt. Express* **13**, 400-409 (2005),
<http://www.opticsexpress.org/abstract.cfm?URI=OPEX-13-2-400>
 40. L. N. Thibos, R. A. Applegate, J. Schwiegerling, R. H. Webb, and VSIA Standards Taskforce Members, "Standards for reporting the optical aberrations of eyes," *J. Refract. Surgery* **18**, 652-660 (2002).
 41. M. P. Cagigal, V. F. Canales, J. F. Castejón-Mochón, P. M. Prieto, N. López-Gil, and P. Artal, "Statistical description of wave-front aberration in the human eye," *Opt. Lett.* **27**, 37-39 (2002).
 42. J. Porter, A. Guirao, I. Cox, and D. R. Williams, "Monochromatic aberrations of the human eye in a large population," *J. Opt. Soc. Am. A* **18**, 1793-1803 (2001).
 43. J. F. Castejón-Mochón, N. López-Gil, A. Benito, and P. Artal, "Ocular wavefront aberration statistics in a normal young population," *Vis. Res.* **42**, 1611-1617 (2002).
 44. L. N. Thibos, X. Hong, A. Bradley, and X. Cheng, "Statistical variation of aberration structure and image quality in a normal population of healthy eyes," *J. Opt. Soc. Am. A* **19**, 2329-2348 (2002).
 45. A. Guirao, J. Porter, D. R. Williams, and I. G. Cox, "Calculated impact of higher-order monochromatic aberrations on retinal image quality in a population of human eyes," *J. Opt. Soc. Am. A* **19**, 1-9 (2002).
 46. A. F. Fercher, C. K. Hitzenberger, G. Kamp, and S. Y. El-Zaiat, "Measurement of intraocular distances by backscattering spectral interferometry," *Opt. Commun.* **117**, 43-48 (1995).
 47. D. Huang, E. A. Swanson, C. P. Lin, J. S. Schuman, W. G. Stinson, W. Chang, M. R. Hee, T. Flotte, K. Gregory, C. A. Puliafito, and J. G. Fujimoto, "Optical coherence tomography," *Science* **254**, 1178-1181 (1991).
 48. W. Drexler, "Ultrahigh resolution optical coherence tomography," *J. Biomed. Opt.* **9**, 47-74 (2004).
 49. W. Drexler, U. Morgner, F. X. Kärtner, C. Pitris, S. A. Boppart, X. D. Li, E. P. Ippen, and J. G. Fujimoto, "In vivo ultrahigh-resolution optical coherence tomography," *Opt. Lett.* **24**, 1221-1223 (1999).
 50. W. Drexler, U. Morgner, R. K. Ghanta, F. X. Kärtner, J. S. Schuman, and J. G. Fujimoto, "Ultrahigh-resolution ophthalmic optical coherence tomography," *Nature Medicine* **7**, 502-507 (2001).
 51. E. J. Fernández and W. Drexler, "Influence of ocular chromatic aberration and pupil size on transverse resolution in ophthalmic adaptive optics optical coherence tomography," *Opt. Express* **13**, 8184-8197 (2005),
<http://www.opticsexpress.org/abstract.cfm?URI=OPEX-13-20-8184>
 52. E. S. Clafflin and N. Bareket, "Configuring an electrostatic membrane mirror by least square fitting with analytically derived influence functions," *J. Opt. Soc. Am. A* **3**, 1833-1839 (1986).

1. Introduction

Adaptive optics (AO) enables the measurement and subsequent correction of optical aberrations in real time. This technology was originally conceived for compensating the degradation induced by the atmosphere over images obtained in ground-based telescopes, in

the context of Astronomy [1]. In recent years, the study of the human eye has also benefited from AO. The eye is a natural target for this technique, since it exhibits time-variable aberrations degrading retinal images [2]. The use of AO in the eye [3] has been devoted to both retinal imaging and to the study of the impact of aberrations in vision. In the first mentioned application, almost all existing ophthalmic modalities have incorporated AO to enhance quality and resolution of the retinal images: flood illumination fundus imaging [4,5], scanning laser ophthalmoscopy [6-8] and more recently, ophthalmic optical coherence tomography [9-13]. Regarding the investigation of the effects and occurrence of aberrations in the eye, AO has also played an important role in the last years [14-20].

The two basic elements in an AO system are the wavefront sensor and the correcting device associated with a calculation kernel. Although different methods have been proposed for measuring aberrations, the Hartmann-Shack wavefront sensor [21], first demonstrated in the eye by Liang and collaborators [22], is the one most widely used in the field [23]. Regarding the aberration correctors, many different devices have been proposed and demonstrated for ophthalmic applications. A first classification can be established into two main groups accounting for the physical principle of operation of the devices: liquid crystal spatial light modulators, using nematic crystal, and deformable mirrors. In the former type, the modulation of the phase is induced by the change of refractive index, consequently affecting optical path, generated in the nematic liquid crystal in response to changes in the applied electrical field [24]. Last generations of these devices, operating in reflection, present several advantages for their use in the human eye [12,25], as a relatively friendly practical implementation and calibration, and a elevated density of independent pixels to generate the required phase profiles. The amplitude or stroke in the programmed phase can be very large. High order aberrations, meaning phase distortions with high spatial frequencies, are possible to be accurately generated with liquid crystal devices. A limitation in the ophthalmic context of liquid crystal correctors is their relatively slow temporal response, in the order of 0.25 seconds. In addition, they required the use of polarized light, and present moderate light absorption. When using polychromatic light, in those devices using phase wrapping, different wavelengths can not be simultaneously modulated.

Deformable mirrors are the other alternative correctors, essentially consisting of a mirrored surface whose shape can be controlled by means of actuators. The mirrored surface can be compounded either by independent mirrors, known as segmented mirrors, or it can be a continuous surface. Segmented mirrors present the drawback of energy losses, caused by the spacing between adjacent segments, and also due to the redistribution of energy arising from diffraction effects from each of the segments. They are the device of choice for primary mirrors in astronomical telescopes endowed with very large diameters. Some advantages of using segmented mirrors are their relatively inexpensive and simple replacement in case of damage, as compared to continuous mirrored face sheets of huge diameter. For ophthalmic applications continuous mirrored membranes are the preferred option. Within this later type, several different deformable mirrors are found depending on how the membrane is deformed, meaning the physical principle shaping the flexible surface.

Deformable mirrors using electroceramic cylindrical actuators, based on the piezoelectric effect, coupled under an aluminized glass face plate surface have been widely used in the eye [4,7,10,26]. This technology shows near hysteresis free operation and very high temporal response (in the order of KHz). The effective stroke is limited to ~ 8 microns and the number of actuators is typically below 100. The actuators can not be densely packed, so relatively wide diameters are required (ranging from 40 to 70 mm). Other bimorph mirrors consisting of a piezoceramic disc bonded to a rigid substrate, with actuators covering a wide area are used for low order aberration correction, due to the reduced number of independent actuators [11,27] (typically < 20). They present larger stroke, but hysteresis becomes important, reducing the fidelity of the device. Electrostatic deformable mirrors have been also demonstrated in the human eye [3,9,14,16,28-32], being one of the most cost-effective approaches so far. In this case, the actuators are essentially electrodes exerting electrostatic force over the deformable membrane. There is virtually no hysteresis, but the amplitude of the

deformation is rather limited (typically $< 6 \mu\text{m}$). Other available correctors are the microelectromechanical deformable mirrors, also proved in the human eye [8,33]. As in the previous type, they use electrical forces to shape the mirrored surface, but to mechanically displace the actuators instead. This approach enables for high packing ratios (~ 1000 actuators in 3-4 mm diameter). With a stroke of 6-8 μm , they exhibit high linearity, no hysteresis and low cost per actuator.

Currently, deformable mirrors available in the market present a limited capability to correct for the ocular aberrations, even in normal eyes. This is especially dramatic when low order aberrations, defocus and astigmatism, are considered. In addition, the cost of the technology is still elevated, especially when thinking in mass incorporation of AO in commercial ophthalmoscopes.

In this work we present a novel deformable mirror, using magnetic force to control the shape of the flexible membrane. This new technology exhibits several advantages in the performance as compared to others. We will characterize and demonstrate the device for ocular applications. Full ocular aberration correction with polychromatic illumination in the near infrared, simultaneous monochromatic and chromatic aberration correction, will be presented by using the magnetic deformable mirror in conjunction with an achromatizing lens.

2. Methods

2.1. Experimental setup

An optical system was designed for testing the magnetic deformable mirror, also allowing for the correction of the ocular aberrations in humans. The experimental setup is compounded by lenses and spherical mirrors. Essentially, the system optically conjugates the exit pupil of the eye, given by the virtual image of the iris through the cornea, with the plane of the deformable mirror, the wavefront sensor, and an achromatizing lens. Conjugation is achieved by using telescopes. These are formed by two positive lenses or by a spherical concave mirror and a positive lens, alternatively. Concave mirrors are free of chromatic aberrations and back reflections, but they introduce some other aberrations when implemented off-axis, mainly astigmatism and coma aberration. All lenses are off-the-shelf achromatic doublets designed for the near infrared.

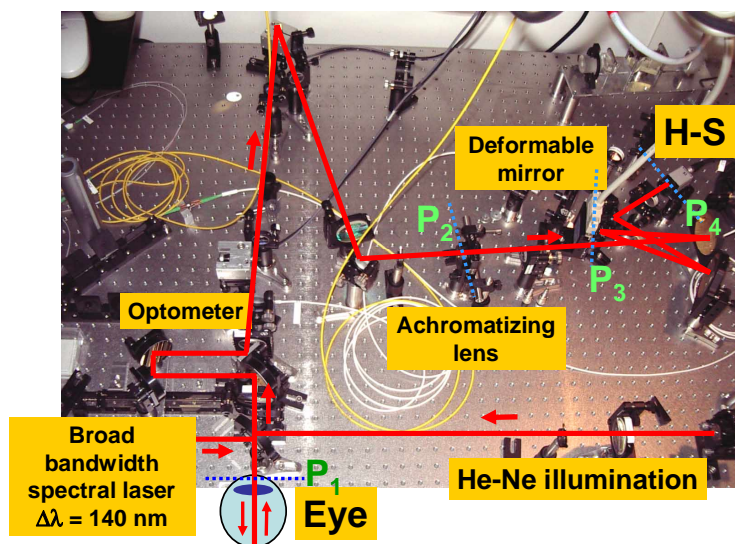


Fig. 1. Picture of the adaptive optics system for the human eye. Planes, optically conjugated are indicated with dotted lines.

Figure 1 shows a picture of the actual system with its main components. In Fig. 1, conjugated planes are indicated with letter P and the direction of the light is shown with arrows. The absolute values of the magnification of the marked planes with the plane of the eye's pupil are 1, 2 and 0.5 for the achromatizing lens, the deformable mirror and the wavefront sensor, respectively. The system accepts an entrance pupil, at the eye's pupil plane, of 7.3 mm diameter.

Two different subsystems are coupled in the setup for illumination. A He-Ne laser emitting at 632.8 nm is used for alignment, introducing a highly collimated, virtually aberration-free, beam into the system. Light is launched into the apparatus through an uncoated pellicle beam-splitter (92 % transmission) placed in front of the eye.

A second arm is used to illuminate the subject's retina via the aforementioned beam splitter, allowing the measurement and correction of ocular aberrations in the system. The light source is a compact, prismless, mode-locked Ti:sapphire laser. This type of Kerr-lens mode-locked lasers produces smooth ultra-broad spectra in the near infrared, with high power and high optical quality. It operates with pulses of 110 MHz, emitting a spectrum of 130 nm FWHM centered at 800 nm [34]. Light from the laser source is launched into a 100 m long monomode optical fiber in order to stretch the pulses. The use of the fiber prevents the femtosecond pulses generated by the laser source to damage the retina, providing dispersive stretching of the pulse duration to hundreds of picoseconds. The effect brings about the reduction of the peak pulse intensities by several orders of magnitude. Due to the fact that the laser operates at a repetition rate of 110 MHz, in practice, exiting light can be considered as a continuous wave [35].

At the other end of the fiber, connected with the experimental apparatus, a triplet lens collimates the beam for the illumination of the eye. The collimator is mounted in a special stage, allowing for three-dimensional positioning. Beam size is limited to 1 mm diameter by using a diaphragm in front of the collimator. Possible corneal reflections affecting the wavefront sensor readouts are avoided during the experiment by displacing the collimator.

The system incorporates a commercial Hartmann-Shack wavefront sensor (HASO 32 OEM, Imagine Eyes) for measuring the ocular aberrations and controlling the deformable mirror. The sensor is compounded by a CCD camera and an array of 32x32 microlenses coupled in the camera's mount, making the device compact and portable. The maximum pupil accepted by the sensor is 3.65 mm diameter, sampling in this case the wavefront with ~ 800 microlenses (the size of each square lens is ~ 0.114 mm). Calibration of the sensor is provided by the manufacturer.

2.2. Magnetic deformable mirror

A novel deformable mirror is used for correcting ocular aberrations. The active mirror consists of a flexible membrane deformed by a set of 52 magnetic actuators. The size of the mirror (without cable and electronic driver) is about 6.9x6.4x2.8 cm. A silver coating gives high reflectivity in both visible and near infrared domains. Figure 2(A) presents a lateral scheme of the magnetic mirror. A voltage applied to the coil creates a magnetic field pushing or pulling the magnet, depending on the sign of the applied voltage. The produced force between the actuators and the flexible membrane is proportional to the magnetic field created inside the coil. The latter is directly proportional to the current in the coil. Consequently, the exerted force from the actuators depends linearly on the applied current in the deformable mirror.

The distribution and ordering of the actuators underneath the deformable membrane is presented in Fig. 2(B). The 52 actuators are placed on a ~ 17 mm diameter area with an inter-actuator spacing close to 2.5 mm. The mirrored surface approximately covers the area given by the discontinuous blue line, 15 mm diameter. According to the manufacturer, the initial flatness of the deformable mirror is below 0.1 μm RMS over the entire pupil. The area used for both testing the deformable mirror and correcting the ocular aberrations is indicated in Fig. 2(B) by a dotted red line. It corresponds to 11.89 mm diameter. This particular diameter was chosen to allow a circular set of actuators to be out of the region of interest. This enables the

edge of the projected pupil for better reproducing higher spatial frequencies. Reducing the control area also decreases the amplitude or stroke of the deformation in the membrane.

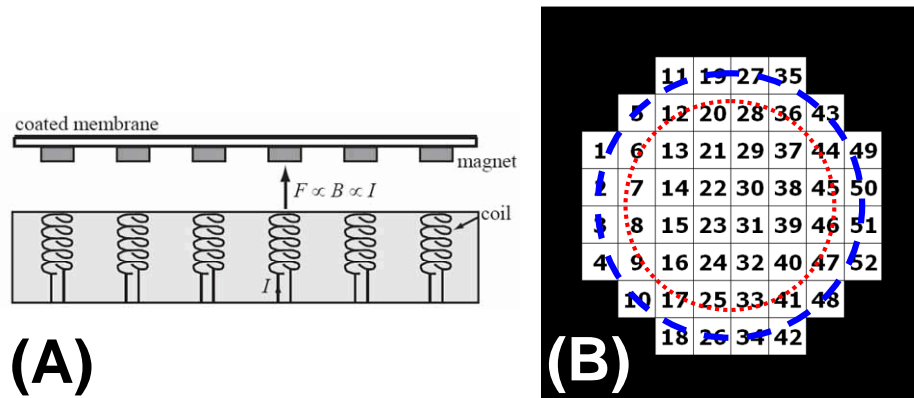


Fig. 2. (A) Scheme of the Mirao 52. Magnets are fixed under the reflecting deformable membrane. A corresponding set of coils, creates magnetic fields pushing or pulling the magnets, depending of the voltages applied to the coils. (B) Distribution of the actuators underneath the deformable membrane in the magnetic mirror. Dashed line shows the mirrored area (15 mm diameter), while the dotted circle, corresponding to 11.89 mm diameter, is the selected area for characterizing the deformable mirror.

The mirror is driven by a 2 level electronic driver: the first one receives the computed numerical information from the computer, coding the voltage values, and processes them to analog values. The second stage, mainly composed with 52 amplifiers, amplifies and addresses the 52 analog voltages to the coils.

2.3. Close loop driving procedure

The control of the loop is accomplished by using a commercially available program (HASO CSO, Imagine Eyes), which includes all the required drivers to handle the deformable mirror and the wavefront sensor. The control of the surface of the membrane is accomplished by sending appropriated voltages to each actuator from the driver. This driver is connected to the computer, from where the values of the signals are initially sent. The surface to be reproduced by the membrane has to be translated to a set of voltages. The control procedure in this work is based in the initial measurement of the influence functions of the mirrored surface. These correspond to the response of the membrane to the action of every isolated actuator, activated with a known voltage. The measured surfaces for each actuator are grouped in the so-called influence functions matrix. Assuming a linear response of the membrane, the control matrix of the membrane, being the function translating required surfaces to set of voltages, is obtained by inverting the influence function matrix. Since this matrix is normally neither square nor regular, meaning that some columns could be linear dependent, regular inversion is usually not possible. Singular value decomposition (SVD) of the influence functions matrix is a relatively simple algebraic method proposed and demonstrated for solving these types of inversions [21,32,36,37]. In addition, the method provides a finite base (whose maximum dimension equals to the number of independent actuators) of orthogonal functions, or surfaces, for the infinite set or family of surfaces which can be exactly reproduced by the membrane. Once the control matrix is calculated, the algorithm to reproduce or correct a given wavefront is straightforward.

Each loop step can be described as follows: the measured wavefront is compared to the selected target wavefront. The difference, called residual, is multiplied by the control matrix, obtaining a set of voltage increments. These increments are added to the previous applied voltage set. Before summation, the increments are attenuated by a gain factor, preventing

overshooting of the signal which might cause instability and divergence. Working with increments prevents divergence due to a wrong wavefront measurement, perhaps produced by blinking etc. The procedure is repeated continuously, in closed-loop, until the residual is stabilized to the smallest possible value.

2.4. Achromatizing lens

The system incorporates an achromatizing lens (AL) for the static correction of the longitudinal chromatic aberration of the human eye. The design and the capabilities of the lens have been reported in a previous work [38]. The lens is a cost-effective symmetrical triplet made of two different glasses only, flint-crown-flint, specifically designed for the near infrared range, from 700 to 900 nm. The design induces virtually no other aberrations but defocus. It exhibits near zero power at 800 nm, the central wavelength of the spectral range used in this work. The AL essentially introduces the opposite average value of longitudinal chromatic aberration typically found in normal eyes [39]. The correction and benefits of the chromatic aberration by using this AL have been demonstrated by using a Hartmann-Shack wavefront sensor and a broad bandwidth laser light source [38].

The particular design of the AL requires the use of absolute magnification 1 with respect to the eye's entrance pupil. Placing the lens directly in front of the eye is also possible, instead of in a conjugated plane, although in this case perfect conjugation can not be achieved. Correct alignment of the lens with the eye's pupil is critical. The location of the AL in a conjugated plane also makes this operation easier in practice.

2.5. Experimental procedure

Five subjects between the age of 30 to 40 years (S_{1-5} , average: 34 yrs; standard deviation: 5 yrs), participated in the measurements. Infrared illumination from the mode-locking pulsed laser is launched into the eye for measuring ocular aberrations. Intensity of the light is always kept below 40 μW , matching safety standards of maximum laser exposure in more than one order of magnitude [35]. Measuring rate and closed-loop operation is set to 8 Hz, although faster operation is in principle possible. Frequency is only limited by the camera readout velocity and the computer microprocessor capabilities. Pupil is limited to 6.6 mm diameter. Eyes are artificially dilated with cyclopentolate 0.5 % at the beginning of the runs. Subjects are fixed to the system by using a bite-bar with their dental impression, mounted in a three-dimensional stage allowing for accurate centering.

3. Results

3.1. Influence functions

In order to characterize the capabilities of the mirror, the influence functions matrix is first obtained in a pupil of 11.89 mm diameter. These functions are the responses of the membrane to a given voltage applied to every actuator. The range of voltage in the device is ± 1 V. The voltage is limited by the driver, preventing the device to be exposed to larger absolute voltages, which might permanently damage the deformable membrane. The available software enables different voltages to be sent to the actuators in a controlled manner. Possible residual aberrations in the system affecting the estimation of the response of the membrane are avoided by using a reference wavefront, recorded applying zero voltage to the entire set of electrodes.

Figure 3 shows three aberration maps generated by three different actuators: 31, 40 and 48, from top to bottom. The estimation of the wavefront is performed through the Zernike polynomials expansion, using the normalization and ordering given by the OSA standard for ocular aberrations [40], up to the sixth order. The center of actuator 48 does not lie on the measured area, but its effect is also important since it affects the edge of the pupil, where most of the aberrations are located in the human eye. The election of this particular set of actuators covers a diagonal section in the membrane, starting from the center towards the periphery. This set of actuators is intended to be representative for the study of the response of the

membrane at different eccentricities. In the left column of Fig. 3, a color-coded, two-dimensional representation of the measured wavefront is presented, obtained by applying 0.5 V to each selected actuator. The dotted white line indicates the direction of the plane where the profile of the wavefront is estimated. The right column depicts, in different colors, the membrane's profiles as a function of the aperture of the deformable mirror. They are measured as a response of voltages 0.25, 0.5, 0.75 and 1 V applied over each actuator. The axis scales in the 3 plots are identical, to allow direct comparison between the responses. The amplitude of the deformation in the membrane decreases with the eccentricity of the considered actuator. The shape of the wavefront is very similar among different applied voltages, qualitatively showing a linear response of the membrane.

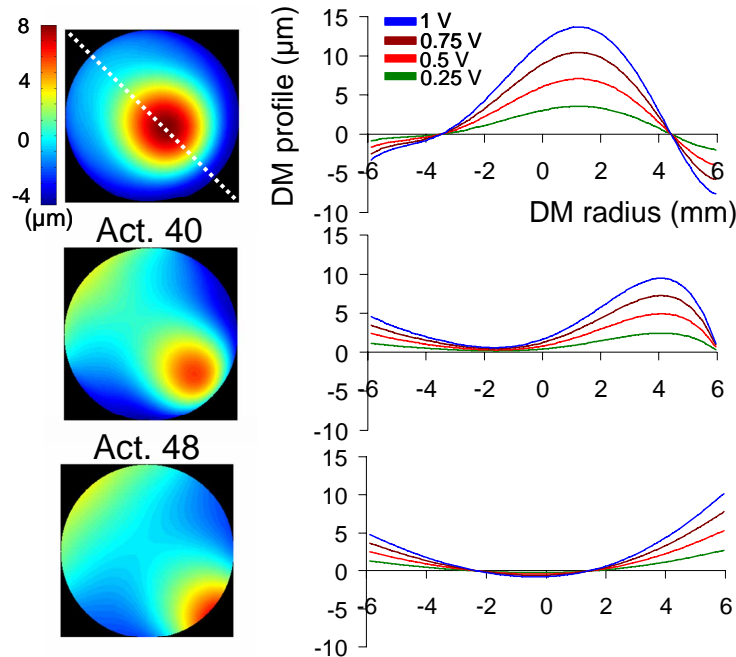


Fig. 3. Selected influence functions of the deformable membrane. Right column shows the profiles, obtained by applying different voltages, of the mirror extracted from the diagonal of the corresponding wavefront maps.

This apparent linearity in the response of the membrane is studied with more detail in Fig. 4. Measured deformation of the membrane, in terms of the peak-valley value, for every actuator in different colors as a function of the applied voltage is presented in Fig. 4. The solid points correspond to the obtained deformation, while the dashed lines are the corresponding least square linear fits performed over every set of data. Figure 4 depicts the whole available range of possible voltages. The linear fits are enforced to cross the zero value, since the sensor retrieves a totally plane wavefront in absence of voltage (by using a reference wavefront). The obtained linear equations are also displayed. In all cases, the square of the linear correlation coefficient is 0.999, indicating a near perfect linear fit. This characteristic of the device, allowing the deformation induced by an actuator to be accurately predicted, makes the deformable mirror suitable for possible open-loop operation, provided that a previous calibration is accomplished.

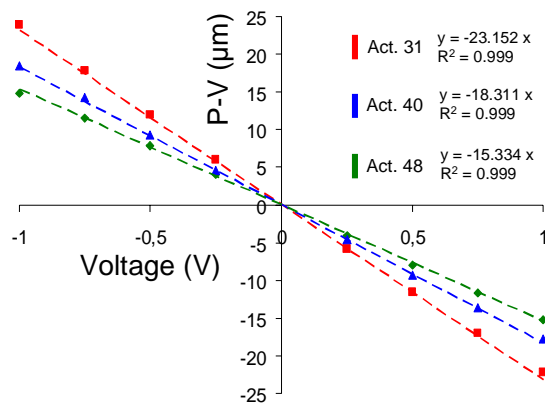


Fig. 4. Peak-valley values obtained from some selected influence functions as a function of the applied voltage. Dashed lines are the corresponding linear fits performed over each set of data. Estimated linear equations and regression coefficients are also displayed in the graph.

3.2. Zernike polynomials generation

The number of actuators and the physical response of the membrane, in terms of the amplitude range that can be induced, limit the capability of the device to reproduce different surfaces. In this context, the orthogonal set of Zernike polynomials is widely utilized to describe wavefront aberrations. These polynomials, up to the fifth order, were systematically reproduced by the membrane in order to characterize the range and the quality of their production.

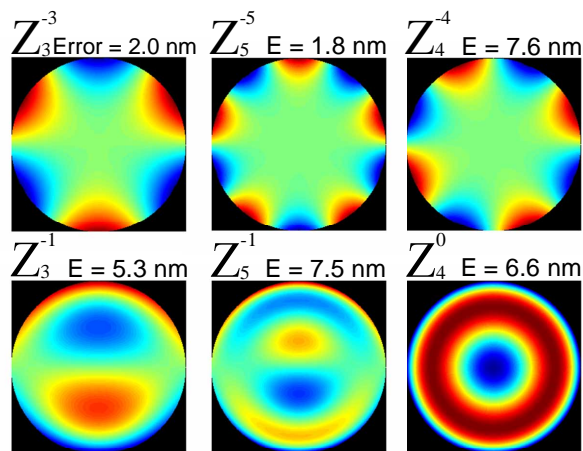


Fig. 5. Selected Zernike polynomials generated by the deformable mirror measured by the Hartmann-Shack wavefront sensor. In all cases, $1 \mu\text{m}$ is programmed for the production of the polynomial. The error, being the difference between the intended coefficient and the measured RMS, is also presented over each aberration map.

Figure 5 shows color-coded representations of some polynomials generated in closed-loop by the membrane, as they are estimated by the Hartmann-Shack wavefront sensor. In all the examples presented in Fig. 5, the value of the coefficient for the target polynomial is set to $1 \mu\text{m}$ in a pupil of 11.89 mm diameter. Blue and red color indicates most negative and

positive values, respectively. The difference of the programmed polynomial and the actually measured one by the sensor, the error or deviation of the generation, is shown on top of each plot. The errors are notably small, ranging from 1.8 to 7.6 nm, showing an excellent accuracy in the generation of these polynomials. In addition, the two-dimensional aberration maps qualitatively show that there are no other spurious polynomials appearing associated to the programmed ones. These coupled polynomials are a well known problem typically occurring with deformable continuous membranes in the generation of surfaces, previously studied in the case of Zernike polynomials [32]. This effect is referred to as mode coupling or cross talk. Mode coupling manifests due to the fact that the base of the deformable membrane, the minimum set of independent functions that can be exactly reproduced by the flexible surface is finite, previously discussed in methods. Therefore, the set of Zernike polynomials can never be perfectly reproduced. In order to establish the actual fidelity of the generation of the Zernike polynomials, the first 20 terms, covering up to the fifth order, were systematically induced in the deformable membrane. A first evident limit in the range of production of the Zernike polynomials is given by the maximum and minimum voltages that can be applied to the device, ± 1 V.

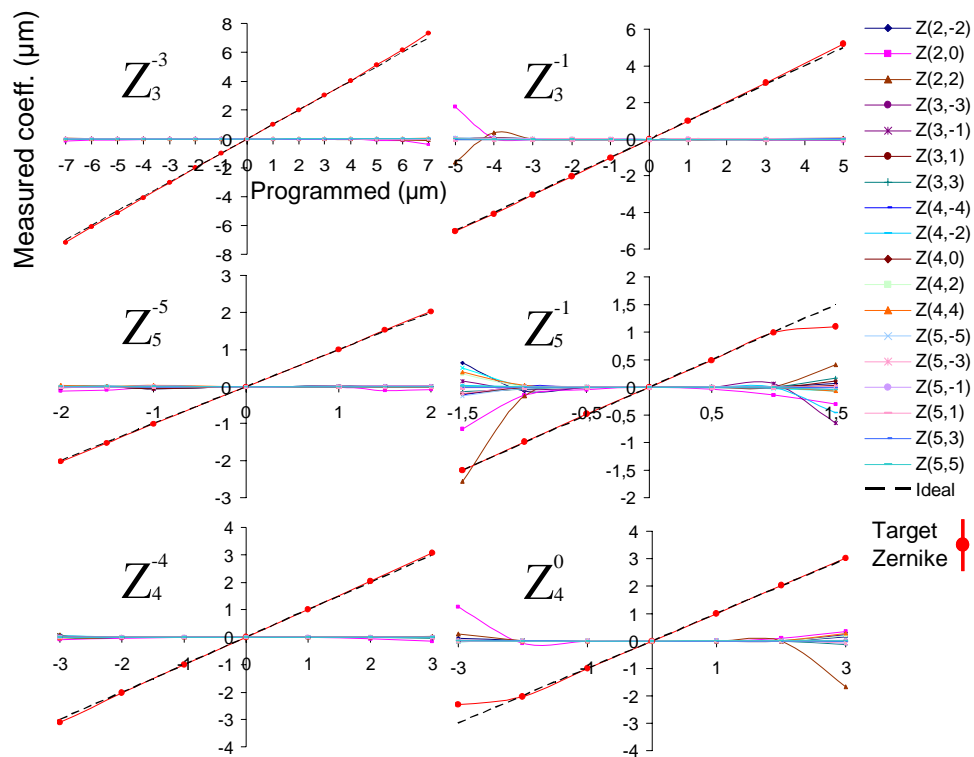


Fig. 6. Mode coupling and fidelity of the magnetic deformable mirror in the generation of some representative Zernike polynomials. Polynomials up to the 5th order are shown in all cases. Dashed lines correspond to the ideal response.

Figure 6 shows the obtained results for the polynomials previously presented in Fig. 5. The graphs plot the measured Zernike polynomials up to the fifth order during the generation of some selected terms, indicated with red color. The ideal response is shown with a black dashed line. Trefoil, polynomial $Z(3,-3)$ is presented at the top left side. For this particular polynomial, mode coupling is virtually zero within the range of permitted voltages. Fourth and fifth order trefoils, $Z(4,-4)$ and $Z(5,-5)$, manifest mode coupling towards the end of the

range, although the amount is still practically negligible. Right column in Fig. 6 shows third and fifth order coma aberrations, $Z(3,-1)$ and $Z(5,-1)$, together with spherical aberration, at the bottom, $Z(4,0)$. The case of $Z(3,-1)$ presents an asymmetric trend, exhibiting a more marked mode coupling towards negative values. In particular, certain amounts of defocus and astigmatism, $Z(2,0)$ and $Z(2,2)$, appear in the plot. Nevertheless, the fidelity of the production of the term, the value of the intended coefficient, still remains near perfect, even in the vicinity of limits. The range of production of fifth order coma aberration is notably smaller than in the previous term, appearing a more evident mode coupling in this case. Finally, the plot for the spherical aberration also shows mode coupling near the borders of the range, essentially defocus and astigmatism. Similarly to the rest of the presented cases, there is a range where mode coupling is practically zero and the accuracy of the generated polynomial is very high.

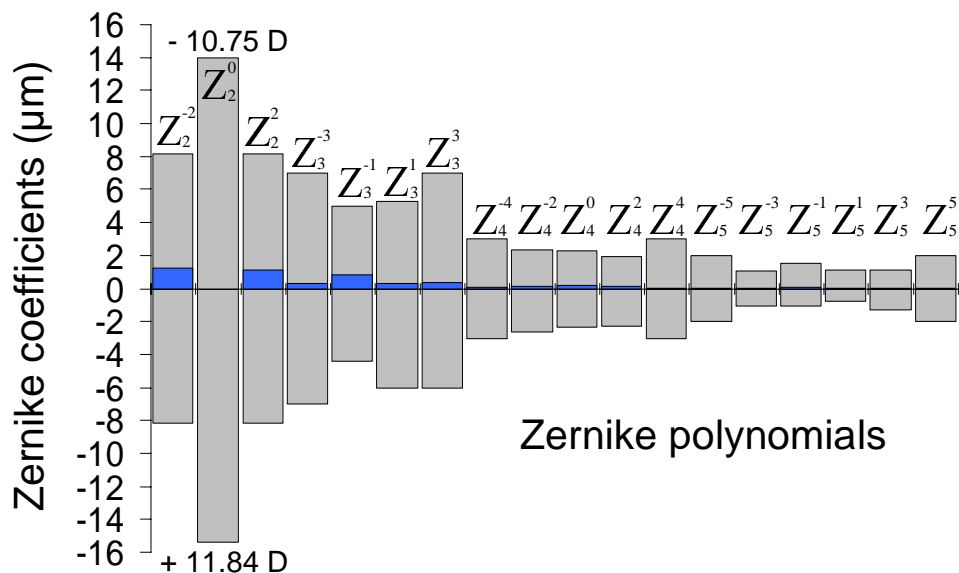


Fig. 7. Experimental ranges of Zernike polynomials production up to the 5th order in the deformable mirror, allowing an error below 5 % in the fidelity of the generation. Dark blue bars correspond to absolute average values of Zernike polynomials found in keratoconic eyes (adapted from Guirao et al., 2002) [45].

Therefore, a polynomial can be considered to be correctly generated when the value of the corresponding coefficient is similar to the programmed one, and the rest of terms, arising as a consequence of mode coupling, are comparatively small. A possible and straightforward approach to establish a criterion for well generated Zernike polynomials is the use of the total root mean square (RMS) of the measured wavefront. Global RMS can be compared with the value of the intended Zernike polynomial coefficient. In this section, a maximum threshold of 5 % in the difference between the measured RMS and the value of the programmed coefficient is established. The selected limit of 5 % might appear as too restrictive in certain practical cases. However, it assures a high fidelity of the generated Zernike polynomial for characterization purposes. The results obtained with this criterion are presented in Fig. 7, where the first Zernike polynomials up to the fifth order, excluding piston and tilts, are depicted in a bars diagram. In the case of pure defocus, given by $Z(2,0)$, the value of the coefficient in diopters has also been included, calculated for an hypothetical pupil size of 6 mm diameter, a feasible size in the human eye.

The obtained ranges for the Zernike polynomials can be confronted with those typically found in the human eye, in order to characterize the performance of the device for visual applications.

Due to the huge variability among subjects, there is no a simple structure function, as it is the case in astronomy to describe the effect of atmospheric turbulence over light incident on the ground-based telescopes, to model normal aberrations of the human eye. Some attempts trying to describe such a function have been reported in the past, concluding that the eye can be understood as a statistically homogeneous medium [41]. Several works have measured the aberrations of normal eyes in large (statistically significant) populations, in order to determine normal ranges of occurrence [42-44]. The amplitude obtained in the current work in the Zernike polynomials, including those terms describing defocus and astigmatism, is clearly superior to the ones found in normal eyes, even in some cases presenting values of more than one order of magnitude larger. In order to provide some graphic comparison, we have used the ocular aberrations reported by Guirao and collaborators [45] from some pathologic eyes. The mean absolute values obtained from eight keratoconic eyes in a pupil of 5.7 mm diameter, excluding defocus, adapted from the aforementioned work, have been presented in the bars diagram of Fig. 7 with dark blue color. Keratoconus is a degenerative condition of the cornea, causing a dramatic change in its shape and thickness. The distortion caused by the reshaped cornea, typically increasing high order aberrations, can in some cases impair tremendously the perceived images. Note that in the Fig. 7, the Zernike polynomials of the keratoconic eyes up to the fifth order are presented, but the scale does not allow to resolve all of them due to their small value compared to the ones generated by the deformable mirror.

Once the performance of the deformable mirror has been studied, especially regarding the production of Zernike polynomials, aberration corrections obtained in real eyes will be presented in the next section.

3.3. Aberration correction in the human eye

In the setup monochromatic aberrations are compensated by the deformable mirror while ocular longitudinal chromatic aberration is corrected statically by the achromatizing lens.

Left part of Fig. 8 shows the average effect over the chromatic defocus, measured by a Hartmann-Shack wavefront sensor, of the achromatizing lens in four subjects (subject S3 was not included in these measurements). The spectral bandwidth is 140 nm centered at 800 nm. Natural case in the Fig. 8 refers to the chromatic defocus recorded without the achromatizing lens. Measurements were obtained under cyclopegia and they have already been described elsewhere [38]. Error bars show the standard deviation. Figure 8 shows an average near perfect correction (close to the sensitivity of the wavefront sensor) of the longitudinal chromatic aberration when using the achromatizing lens. Right side of Fig. 8 depicts the benefit of the correction of the chromatic aberration in absence of monochromatic aberrations, the hypothetical case with an ideal deformable mirror. The polychromatic point-spread functions (PSFs) in the case of no chromatic aberration, labeled as perfect, and including the effects of the chromatic aberration (CA), are also presented for a pupil of 6.6 mm diameter. The simulation of the defocus in the PSFs is accomplished by using the semi empirical expression obtained by Fernández and collaborators [39] describing ocular chromatic aberration in the near infrared. The spectral distribution is assumed to be Gaussian, in order to emulate the actual spectrum emitted by the light source employed in the experiment (FWHM 140 nm centered at 800 nm). Consequently, the different PSF at different wavelength are weighted by a Gaussian function, reducing the effective contribution of those wavelengths located at the tails of the spectrum. For the calculation of the polychromatic PSF is also necessary to take into account the inherent scaling of the diameter of the PSF as a function of wavelength. The energy of the intensity distribution has to be normalized in order to make PSF at different wavelengths comparable before summation. The modulation transfer functions (MTFs) shown in the right panel are calculated from the estimated PSFs. The red curve corresponds to the case affected by ocular chromatic aberration. This curve shows a notable decrease of the optical quality, in both contrast and resolution, as compared to the

perfect case (in blue color). Note that the red curve establishes the limit for a perfect aberration correction in the eye under polychromatic illumination. The use of the achromatizing lens is intended to overcome this limitation, enabling the system to really reach an optical quality close to the perfect case (blue line in Fig 8).

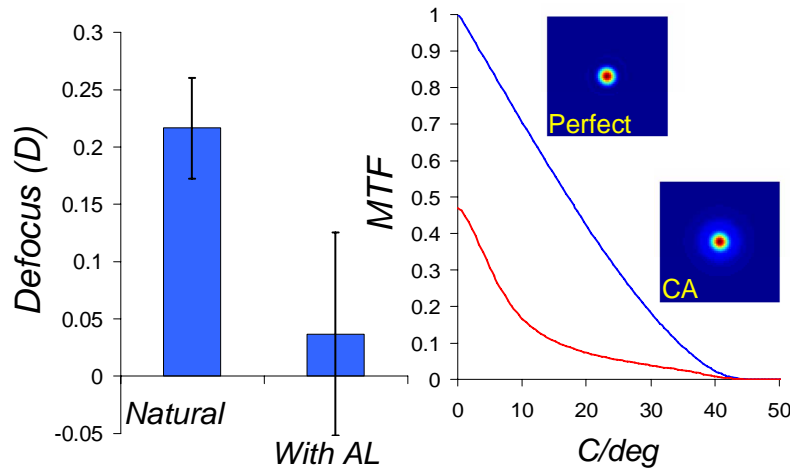


Fig. 8. Left panel: average longitudinal chromatic aberration obtained from 4 subjects, using a Gaussian spectrum 140 nm FWHM centered at 800 nm, with and without the achromatizing lens (with AL and natural respectively). Right panel: effect of the ocular chromatic aberration over the modulation transfer function in absence of monochromatic aberrations for a pupil of 6.6 mm diameter. Red color indicates in the plot the case affected by chromatic aberration (CA). Polychromatic point-spread functions with and without ocular chromatic aberration are presented.

Aberration corrections accomplished by the magnetic deformable mirror and the AL are presented and studied in the following.

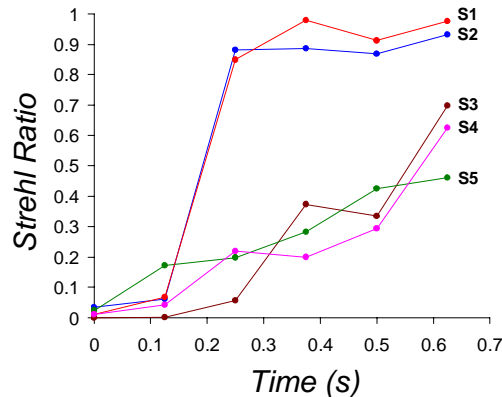


Fig. 9. Temporal evolution of the Strehl ratio from 5 different eyes during closed-loop aberration correction in a pupil of 6.6 mm diameter.

Figure 9 shows the evolution in time of the Strehl ratio during the aberration correction in every subject, obtained at 8 Hz in a pupil of 6.6 mm diameter. Strehl ratio is calculated as the ratio between the peak of the actual PSF measured during the correction and the ideal value obtained in the case of an aberration-free eye with an identical pupil size. Consequently, the

value 1 indicates a perfect aberration correction. The first six iterations, corresponding to 0.625 seconds, of the closed-loop aberration correction procedure are shown. Figure 9 exhibits different trends in the evolution of the correction across subjects. While in subjects S1 and S2 near perfect aberration correction is accomplished in 2 iterations, other subjects exhibit a more moderate slope, indicating that a higher number of iterations are required to fully correct the aberrations in these cases. Subjects S1 and S2 achieve full aberration correction in 0.375 and 0.25 s. However, for subjects S3, S4 and S5 the time required for the correction is 0.625, 0.75 and 0.875 s, respectively. The gain of the algorithm for closing the loop is in all cases 0.5. The velocity of the correction appears as a parameter virtually independent of the initial optical quality of the eye, which can be estimated from the initial Strehl ratios, first points in the graph. The eye movements are the main limitation to the increase of the Strehl ratio, due to the relatively moderate speed of the loop. A good eye fixation quality is mandatory to achieve perfect correction with the current loop velocity.

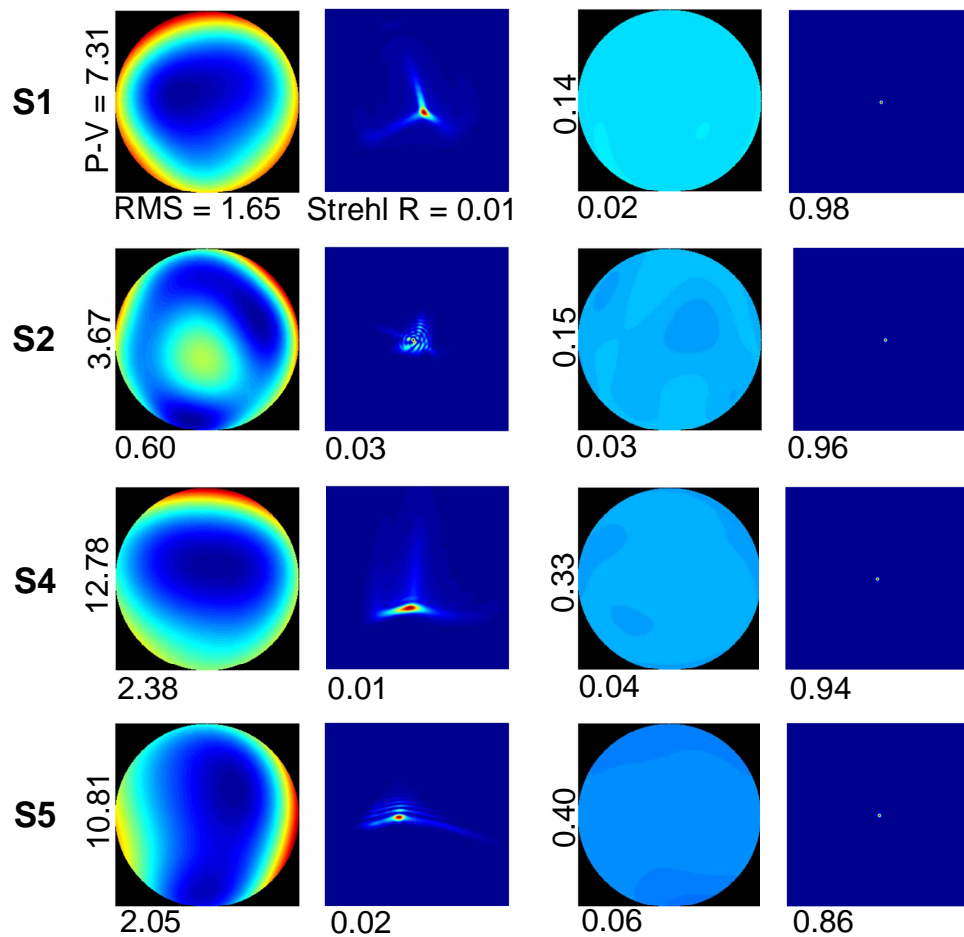


Fig. 10. Left column: initial aberrations and associated polychromatic point-spread functions obtained from 4 real eyes. Right column: best corrected wavefront achieved for each case during the first 1.25 seconds of closed-loop aberration correction. Peak-valley and RMS in microns for every aberration map are displayed at the left and bottom of the maps respectively. Strehl ratios are also included below every point-spread function.

The aberration correction is further studied in Fig. 10, where initial aberrations (left column) and the best corrections (right column) achieved for each subject are presented. Color-coded aberrations maps, where blue and red colors indicate negative and positive values respectively, estimated by the wavefront sensor are depicted. In order to provide the scale in the color-coded maps, the values of the maximum deformation of the wavefront are given in every case. This is indicated with the peak-valley parameter (P-V, given in microns), at the left side of the maps. The aberrations are retrieved up to the sixth order using the Zernike polynomials expansion. The values of the RMS (in microns) are posted under the maps.

The associated polychromatic PSFs, presented at the right side of the maps, are estimated in the uncorrected case assuming the average chromatic aberration typically found in normal eye and a Gaussian spectrum centered at 800 nm, in a totally similar manner as it has been described for the right panel of Fig. 8. In the representation of the PSF, blue color indicates zero while red corresponds to the maxima of energy for each case. Data from subject S3, suffering of myopic defocus, are presented in Fig. 11 for a more detailed analysis. The corrected cases are chosen among the first 1.5 sec of the closed-loop aberration correction, as the ones exhibiting the largest Strehl ratios. The RMS after aberration correction is notably low, ranging from 20 to 60 nm, with high Strehl ratios, in all cases above the diffraction limit. Figure 10 indicates that near perfect monochromatic ocular aberration in different eyes is accomplished with the magnetic mirror.

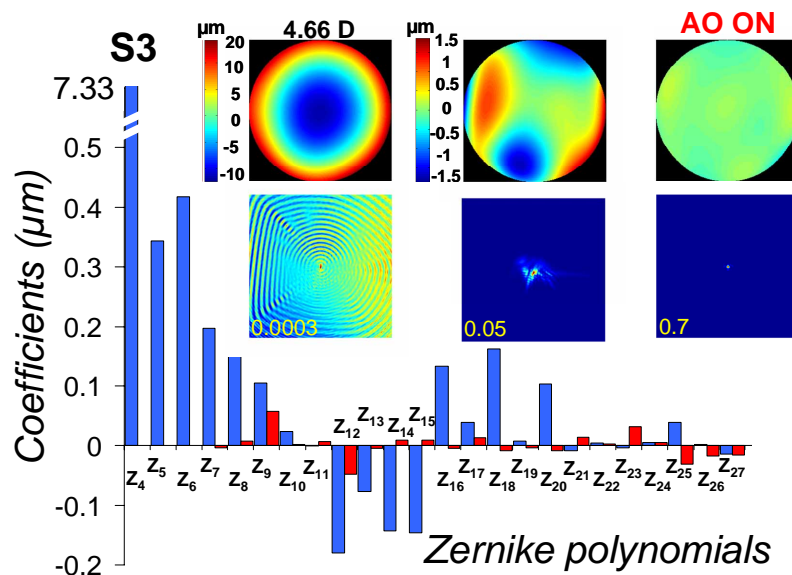


Fig. 11. Aberration correction for subject S3. From left to the right the aberration maps show the initial aberrations, the initial aberrations without defocus and the corrected case respectively. The associated polychromatic point-spread functions are displayed below every aberration map together with the Strehl ratio. The bars diagram shows the Zernike coefficients in the natural case, in blue color, and after aberration correction, in red.

Subject S3, not included in Fig. 10, presents a notable myopia (4.66 D, measured with the Hartmann-Shack wavefront sensor) and a rather irregular cornea that introduces high order aberrations, above normal ranges reported in previous works [42-44]. This particular case is depicted in Fig. 11. The color-coded aberration maps show, from left to right side, the initial aberration, the initial aberration excluding defocus, and the residual after correction by the deformable mirror. The color bars indicate the scales. Note that the initial aberration presents more than 30 μm peak-valley. Below the aberration maps, the associated polychromatic PSFs are depicted together with their Strehl ratios. The PSF corresponding to the initial aberration, because of the large defocus, is only partially shown. The same sampling is applied in the

Fourier transform for the estimation of the PSF from the wave aberration in all cases. In the corrected case, a Strehl ratio of 0.7 is achieved, showing a tremendous increase in the optical quality of the eye as compared to the natural case. The bars diagram explicitly shows the values of the different aberration terms before and after closed-loop aberration correction up to the sixth order, in blue and red color respectively. The aberration map corresponding to the initial case, with no defocus, shows a valley-like structure at the bottom, which might indicate a developing keratoconus in its early stage, producing a significant increase of high order aberrations, which can be noticed in the bars diagram. After aberration correction, the remaining aberrations are small, including those corresponding to high orders (fourth and fifth, particularly important in this subject).

4. Conclusions

4.1. Full aberration correction

To the best of our knowledge, full aberration correction in the human eye, including both monochromatic and chromatic aberrations, is demonstrated for the first time. This new approach has been previously referred to as pancorrection, meaning complete or full correction, using the Greek prefix pan- [38].

This aberration correction modality might particularly benefit those ophthalmic techniques using polychromatic light sources, like in the case of optical coherence tomography (OCT) [46-48]. In OCT, axial resolution is governed by the spectral width of the light source, while transverse resolution is given by the quality of the spot focused onto the retina. The use of ultra-broad bandwidth spectral light sources in OCT, known as ultrahigh resolution (UHR) OCT [49,50], enables up to 2-3 μm axial resolution in the living retina (using Gaussian-shaped spectra of 130 nm FWHM in the near infrared, similar to the case studied in the current work). Recently, limits to the performance in OCT when using wide pupils and broad spectral light sources have been established [51], showing the necessity of full aberration correction in order to achieve isotropic resolution. The simultaneous correction of both monochromatic and polychromatic aberrations presented in this manuscript provides the experimental demonstration of the concept. But the use of full aberration correction is not limited to the case of OCT. Other ophthalmoscopic modalities, as flood illumination fundus imaging and scanning laser ophthalmoscopy, could also benefit from the use of broad bandwidth light sources, reducing the degradation of the retinal images associated with speckle. Consequently, full aberration correction might also be of interest in those other techniques.

The simultaneous correction of monochromatic and chromatic aberrations presented in this work in the near infrared can be accomplished in other spectral ranges, for instance in the visible. In principle, achromatizing lenses can also be designed to operate in this portion of the spectrum. In this spectral range, the benefit of the chromatic aberration correction should be larger as compared with that in the near infrared, due to the larger chromatic aberration existing in this portion of the spectrum. In this case, and as a possible example of application, the proposed correction can be devoted to the study of the influence of the aberrations in vision, permitting the use of white light.

4.2. Magnetic deformable mirror

The studied magnetic deformable mirror exhibits a highly linear behavior with the applied voltage, contrary to the case found in other deformable mirrors using continuous membranes. This is a notable different characteristic of the presented correcting device as compared to deformable mirrors electrostatically driven. In these last mirrors, Poisson equation describing the force exerted by the actuators over the membrane yields a square dependence with the voltage applied over the actuators [52]. This is also the situation occurring with piezoelectric deformable mirrors.

Another characteristic of the magnetic deformable mirror is its ability to accurately reproduce Zernike polynomials. Although the undesired effect of mode coupling is inherent to

the fact of working with a limited number of actuators and a continuous membrane, the presented correcting device shows a notably high performance, probably due to absence of constraints at the edge of the deformable membrane, and because of the particular elastic properties of the membrane.

Other correcting devices, as liquid crystal spatial light modulators (LC-SLM) have been also characterized in the context of ocular applications, studying the fidelity of the generation of some Zernike polynomials [25]. In particular, in the work of Prieto and collaborators the fidelity of a LC-SLM is explicitly shown, together with the associated mode coupling for certain Zernike polynomials. Third order coma and fifth order trefoil can be directly confronted with those presented in the current work. The range of generation and the fidelity are comparable in these cases, although the technology is completely different. In the case of liquid crystal correcting devices the production of aberrations is accomplished by phase wrapping, using pixels totally independent to each other. Therefore, mode coupling appears as an effect associated to the finite number of available independent pixels (near to 600000 in the commented case) to perform the phase wrapping operation.

The ranges of generation of Zernike polynomials makes the magnetic deformable mirror suitable for ophthalmic applications, being able to fully compensate for the aberrations in normal populations, even covering pathologic cases where ocular aberrations are dramatically increased, as it is the situation in the keratoconic eye. The fidelity of the response of the device allows the use of very high gains in closed-loop, reducing the number of iterations to accomplish aberration correction.

The temporal response of the deformable mirror during ocular aberration correction presents some differences among subjects, as it has been depicted in Fig. 9. Initial degree of aberrations is not correlated with the evolution of the correction; otherwise these are totally within the amplitude capabilities of the deformable mirror. The differences might arise instead from the different dynamics of the eye among subjects, or the stability of the subject during the runs. This could be partially solved by applying different gain factors, experimentally determined for each particular subject, or even incorporating a time variable gain in the closed-loop algorithm.

A notable advantage of this mirror as compared with others is the capability to reproduce large amount of aberrations, including high orders (in this work we have characterized up to the fifth order). The practical use of the deformable mirror in a rather aberrated eye has been demonstrated, showing a good performance even in this case (Fig. 11). In addition to high orders, the magnetic mirror also enables the simultaneous correction of defocus and astigmatism, routinely performed in other systems with trial lenses or additional piezoelectric deformable mirror only handling low order aberrations. In this direction, the presented device might solve the paradoxical situation occurring in some ophthalmic AO systems: despite sophisticated methods are used to correct high order ocular aberrations, known to be of relative importance in moderate pupils and normal eyes, defocus and astigmatism are still corrected by using regular trial lenses.

The limited stroke of deformable mirrors using other existing technologies, in particular when reproducing high order aberrations, makes AO so far a technology suitable for relatively good eyes, meaning normal or low aberrated eyes. In this scenario, highly aberrated eyes, perhaps resulting from pathologic corneas, or simply those affected of large amounts of defocus or astigmatism, have to be excluded for the use of AO. However, aberrated eyes are precisely those which should benefit more from AO. In this scenario, the presented magnetic deformable has been demonstrated to fulfill the requirements for its use in the human eye.

Acknowledgments

Laurent Vabre is grateful to the Region Ile de France for a post doctoral fellowship.

This research was supported in part by Cardiff University, Wales, UK; FWF Y159-PAT; the Christian Doppler Society; FEMTOLASERS Produktions GmbH, and Carl Zeiss Meditec AG.

W. Drexler, the corresponding author, can be reached at: DrexlerW@cardiff.ac.uk